Three-dimensional magnetotelluric modelling in a mixed space-wavenumber domain

Shikun Dai[1], Dongdong Zhao[2], Shunguo Wang[3], Kun Li[4], Hormoz Jahandari[5]

1 School of Geosciences and Info-physics, Central South University, Changsha, China.

2 School of Electronic Engineering and Automation, Guilin University of Electronic Technology, Guilin, China.

3 Department of Electronic Systems, Norwegian University of Science and Technology, Trondheim, Norway.

4 School of Geoscience and Technology, Southwest Petroleum University, Chengdu, China.

5 Department of Earth Science, Memorial University of Newfoundland, St. John's, Canada.

ABSTRACT

A new three-dimensional (3D) magnetotelluric (MT) modelling scheme in a mixed space-wavenumber domain is presented. The modelling scheme is based on using two-dimensional Fourier transform along two horizontal directions to solve a vector-scalar potential formula derived from Maxwell's equations based on the primary-secondary potential separation. The derived one-dimensional (1D) governing equations in a mixed space-wavenumber domain are solved by using finite element method (FEM) together with a chasing method, and then two-dimensional (2D) inverse Fourier transform is used to recover the final solution of the electromagnetic fields in the 3D spatial domain. An iterative scheme is applied to approximate the true solution by repeating above steps since the governing equations cannot be directly solved due to an unusual primary-secondary potential field separation used. Nevertheless, the new method is capable of reducing the memory requirement and computational time in the mixed domain, and the 1D governing equations are highly parallel among different wavenumbers. For each of the 1D equations, the two- or four-node Gaussian quadrature rule can be utilized in

both horizontal directions for Gauss Fast Fourier Transform. It is worth mentioning that the linear matrix equation to be solved is a fixed bandwidth system, and the chasing method is more efficient and convenient than solvers with preconditioners for the 1D matrix equations. The reliability and efficiency of the newly proposed method are verified with three synthetic 3D models by comparisons with a classical integral equation solution, an adaptive FEM solution, and a nonadaptive FEM solution. The proposed algorithm will be utilized in electrical resistivity tomography and controlled-source electromagnetic methods in future studies.

Keywords: Magnetotellurics; Mixed space-wavenumber domain; Three-dimensional; Numerical modelling; Fast Fourier transform; Finite element method

INTRODUCTION

The magnetotelluric (MT) method plays an important role in various applications, such as crustal structure studies, environment investigation, and resource exploration. Highly efficient and accurate solutions of three-dimensional (3D) large-scale electromagnetic (EM) equations become practical to simulate observations from geophysical surveys and then solve the EM inverse problem (Zhdanov 2010). Many algorithms have been proposed for 3D MT modelling (e.g., Varentsov 1983, Wannamaker *et al.* 1984, Newman & Alumbaugh 2000, Mitsuhata & Uchida 2004, Egbert & Kelbert 2012, Ren *et al.* 2013, Jahandari *et al.* 2017). From the perspective of solving the EM fields or their potentials, MT forward modelling can be cataloged into two types: (a) the EM-field approach (Mackie et al., 1994; Varilsuha & Candansayar, 2018) and (b) the potential approach (Um *et al.* 2010, Mukherjee &

Everett 2011, Jahandari & Farquharson 2014, Varilsuha & Candansayar 2018). Both approaches can accurately solve the relevant partial differential equations (PDE) derived from Maxwell's equations with consideration of an appropriate boundary condition.

The EM-field approach solves the conventional EM Helmholtz equation consisting of either the electric or magnetic fields as unknown quantities in the spatial domain. The principle of this approach is relatively simple and straightforward, but the main drawback of the EM-field approach is that it will violate the divergence-free condition of current due to the accumulation of round-off errors if an iterative solver is used for simulations with low frequency (Lynch and Paulsen, 1991). The application of the vectorial finite element method (FEM) to the solutions of the E-field (Sugeng, 1998; Liu et al., 2008; Farquharson and Miensopust, 2011; Ren et al., 2013; Grayver and Kolev, 2015; Key, 2016) and H-field (Franke et al., 2007) diffusion equation, however, overcomes those difficulties mentioned above for the EM-field approach.

The potential approach that discretizes the EM problem based on a vector-scalar potential formulation instead of directly using electric and magnetic fields has also been suggested. Various gauge methods have been used in a vector-scalar potential formula, and the potential approach can further be divided into the ungauged approach (Mukherjee and Everett, 2011; Ansari and Farquharson, 2014), Coulomb-gauged approach (Haber *et al.* 2000, Jahandari & Farquharson 2014), Lorenz-gauged approach (Um et al., 2010), and Axial-gauge approach (Varilsuha and Candansayar, 2018). These approaches have two main features: (1) using vector and scalar potentials allows the

69 divergence correction scheme to be included implicitly in the stiffness matrix; (2) there
70 are more nonzero elements in the assembled large stiffness matrix compared to the EM-
71 field approaches. Although the solutions of the vector and scalar potentials are not
72 unique, the corresponding EM fields are, however, unique in the ungauged case.

73 For either the EM-field approach or the vector-scalar potential approach, integral
74 equation (IE) method (e.g., Wannamaker *et al.* 1984, D. B. Avdeev *et al.* 2002, D.
75 Avdeev & Avdeeva 2009, Kruglyakov and Bloshanskaya 2017), finite difference (FD)
76 method (e.g., Varentsov 1983, Mackie *et al.* 1994, Newman & Alumbaugh 1995, Haber
77 *et al.* 2000, Sasaki 2001, Shen 2003), finite volume (FV) method (e.g., Haber *et al.*
78 2000, Haber & Ascher 2001, Streich 2009, Jahandari & Farquharson 2014, Jahandari
79 & Farquharson 2015), and finite element (FE) method (Zunoubi et al., 1999; Nam et
80 al., 2007; Um et al., 2010; Mukherjee and Everett, 2011; Ren et al., 2013; Ansari and
81 Farquharson, 2014; Jahandari et al., 2017) are often selected to solve the Helmholtz
82 equations. Note that an explicit divergence correction is required when using the EM-
83 field approach, and it not only ensures the conservation of currents inside an element
84 but also speeds up the convergence process by reducing the number of iterations for the
85 numerical solution (Mackie et al., 1994; Smith, 1996). Direct solvers (e.g., SuperLU
86 and MUMPS) or iterative solvers (e.g., PETSc and GMRES) can be selected to solve
87 the assembled matrix equation, which also influences the calculation accuracy and
88 efficiency (Saad, 2003; Streich, 2009; da Silva et al., 2012; Jahandari and Farquharson,
89 2014).

90 In 3D MT modelling, computation and memory requirements for field data are

enormous, especially when a large-scale sparse linear system is solved. Therefore, regardless of whether one uses the EM-field approach or the potential approach, further development of 3D MT modelling algorithm should focus on improving computational efficiency while preserving high accuracy. From the perspective of differential equations, we propose to carry out the 3D MT forward modelling by obtaining the solution in a mixed space-wavenumber domain based on the potential approach. This method has been used in gravity and magnetic modelling (Dai et al., 2019). Using the method, the 3D vector-scalar potential PDEs are converted into 1D governing equations with different independent wavenumbers by 2D Fourier transform along two horizontal directions in the Cartesian coordinate system. The 1D governing equations with different wavenumbers support parallel computation on high-performance computers. In the vertical dimension, the accuracy and the efficiency are balanced by increasing the mesh size as the depth increases. For the transformed 1D differential equations, the FEM combined with a chasing approach is applied for an accurate and efficient solution of 3D MT modelling. Since the total electric field is involved in the final matrix equation, an iterative approach is required to approximate the final solution. Three 3D models with different anomalies are used to verify the accuracy and the reliability of the proposed algorithm by comparisons between the proposed method and a classical IE method, a spatial domain adaptive FE method, and a spatial domain nonadaptive FE method.

111 BASIC THEORY

112 **Gauged EM potentials**

113 Assuming the time dependence of $e^{-\mathrm{i}\omega t}$ in the frequency domain, the EM fields

114 satisfy the Maxwell equations

115 $$\nabla \times \mathbf{E} = \mathrm{i}\omega\mu_0 \mathbf{H}, \tag{1}$$

116 $$\nabla \times \mathbf{H} = \mathbf{J}_S + (\sigma - i\omega\varepsilon)\mathbf{E}, \tag{2}$$

117 where **E** and **H** represent the electric field (V/m) and the magnetic field (A/m),

118 respectively, in frequency domain. ω represents angular frequency, i represents the

119 imaginary unit, σ represents the conductivity (S/m), ε represents the dielectric

120 permittivity (F/m), and $\mathbf{J}_s$ only represents the current density (A/m^2). Within the MT

121 frequency band (~10^{-5} to 10^4 Hz), the displacement current is negligible, and the free-

122 space magnetic permeability is $\mu_0 = 4\pi \times 10^{-7}$ H/m.

123 The electric field **E** can be described by a vector potential (**A**) and a scalar potential

124 (Φ) (Haber et al., 2000). Where, **A** is known as the magnetic potential, and Φ is the

125 electric potential. The value **A** is a vector perpendicular to the magnetic induction

126 intensity **B**,

127 $$\mathbf{B} = \nabla \times \mathbf{A}. \tag{3}$$

128 The electric field **E** then can be written in terms of the vector potential **A** and the

129 scalar potential Φ as

130 $$\mathbf{E} = \mathrm{i}\omega\mathbf{A} - \nabla\Phi. \tag{4}$$

131 In terms of the EM potentials, equation 2 can be written as the curl-curl equation,

132 $$\nabla \times (\nabla \times \mathbf{A}) = \mu_0 \mathbf{J}_S + \mu_0 \sigma(\mathrm{i}\omega\mathbf{A} - \nabla\Phi). \tag{5}$$

Using the vector identity $\nabla\times(\nabla\times\mathbf{A})=\nabla(\nabla\cdot\mathbf{A})-\nabla^2\mathbf{A}$ and the Coulomb gauge condition of $\nabla\cdot\mathbf{A}=0$ obtains that equation 5 is equivalent to

$$\nabla^2\mathbf{A}+k^2\mathbf{A}-\mu_0\hat{y}\nabla\Phi=-\mu_0\mathbf{J}_\mathrm{S}. \tag{6}$$

Where $k=\sqrt{\mathrm{i}\omega\mu\sigma}$ is wavenumber in the frequency domain, and $\hat{y}=\sigma$ represents the admittivity when the displacement current is negligible.

The divergence-free condition of current density, $\mathbf{J}=\mathbf{J}_\mathrm{S}+\sigma\mathbf{E}$, is satisfied as $\nabla\cdot\mathbf{J}=0$. Thus, to maintain a divergence-free current density, the auxiliary equation can be written as

$$-\nabla\cdot\mathbf{J}_\mathrm{S}=\nabla\cdot\sigma\mathbf{E}. \tag{7}$$

Through replacing the electric field with the $\mathbf{A}-\Phi$ combination in equation 4, equation 7 can be reformed into

$$\nabla\cdot(\sigma\nabla\Phi)-\mathrm{i}\omega\nabla\cdot(\sigma\mathbf{A})=\nabla\cdot\mathbf{J}_\mathrm{S}. \tag{8}$$

The system of equations for the vector potential $\mathbf{A}$ and scalar potential Φ can be composed of equations 6 and 8 (Haber *et al*. 2000; Badea *et al*. 2001) as

$$\begin{cases}\nabla^2\mathbf{A}+k^2\mathbf{A}-\mu_0\sigma\nabla\Phi=-\mu_0\mathbf{J}_\mathrm{S}\\ \nabla\cdot(\sigma\nabla\Phi)-\mathrm{i}\omega\nabla\cdot(\sigma\mathbf{A})=\nabla\cdot\mathbf{J}_\mathrm{S}\end{cases}. \tag{9}$$

Equation 9 should be solved simultaneously as a coupled matrix equation. There is no gauge freedom after applying Coulomb gauge in this system, since the solution's vector potential $\mathbf{A}$ and scalar potential Φ are unique, unlike the ungauged system (Varilsuha and Candansayar, 2018). The equations of $\mathbf{A}$ and Φ can be utilized for 3D forward modelling of MT, electrical resistivity tomography (ERT), and controlled-source electromagnetic (CSEM) methods by tuning the current density and frequency selection. Meanwhile, only 3D MT modelling is presented in this study to illustrate the

methodology and $\mathbf{J}_s$ term is neglected.

When a secondary potential formulation is used to model MT signals, plane waves can be introduced conveniently by explicitly calculating a set of known primary EM potentials ($\mathbf{A}^p$, Φ^p). The primary potentials can be the responses of a half-space or layered electrical resistivity model. The disadvantage of the secondary EM potentials algorithm is that it cannot be easily used for topography inclusion in 3D EM simulation due to the lack of a direct solution of the relevant primary potentials.

The equation of the primary EM potentials ($\mathbf{A}^p$, Φ^p) can be described as

$$\begin{cases} \nabla^2 \mathbf{A}^p + k_p^2 \mathbf{A}^p - \mu_0 \sigma^p \nabla \Phi^p = -\mu_0 \mathbf{J}_s \\ \nabla \cdot (\sigma^p \nabla \Phi^p) - \mathrm{i}\omega \nabla \cdot \left(\sigma^p \mathbf{A}^p\right) = \nabla \cdot \mathbf{J}_s \end{cases}. \tag{10}$$

The secondary EM potentials ($\mathbf{A}^s$, Φ^s) can be defined according to $\mathbf{A} = \mathbf{A}^p + \mathbf{A}^s$ and $\Phi = \Phi^p + \Phi^s$. Then, by subtracting the primary potentials from the total potentials, the governing equation 9 can be rewritten as

$$\begin{cases} \nabla^2 \mathbf{A}^s + k_p^2 \mathbf{A}^s - \mu_0 \sigma^p \nabla \Phi^s = -\mu_0 \sigma^s \mathbf{E} \\ \nabla \cdot (\sigma^p \nabla \Phi^s) - \mathrm{i}\omega \nabla \cdot \left(\sigma^p \mathbf{A}^s\right) = \nabla \cdot \left(\sigma^s \mathbf{E}\right) \end{cases}. \tag{11}$$

Where

$$\begin{cases} k^2 = k_p^2 + k_s^2 \\ \sigma = \sigma^p + \sigma^s \end{cases}, \tag{12}$$

k_p^2 and k_s^2 are the wavenumbers corresponding to the primary and secondary EM potentials, respectively. Similarly, σ^p and σ^s are the conductivity corresponding to the primary and secondary EM potentials, respectively. $\mathbf{E} = \mathbf{E}^p + \mathbf{E}^s$ is the total electric field, where $\mathbf{E}^p$ is the primary field, and $\mathbf{E}^s$ is the second field. In the process of solving equation 11 for the first iteration, only plane electromagnetic waves $\mathbf{E}^p$ is used to represent $\mathbf{E}$, and the initial value of the secondary field $\mathbf{E}^s$ is zero. Then, the total

field **E** on the right-hand side of equation 11 can be updated iteratively with the sum of the secondary field $\mathbf{E}^s$ and the primary field $\mathbf{E}^p$. The details of the iterative method are shown in the end of this section. Equation 11 is different from the conventional equation used for primary and secondary potential separation. This is because the conventional equation contains the product of total conductivity and secondary potential field (e.g. Badea et al., 2001; Chen and Li, 2019), which is equivalent to complicate convolution after the Fourier Transform.

Equations 9 and 11 as well as their equivalent equations have been used in several studies (e.g., Haber *et al.* 2000, Badea *et al.* 2001, Jahandari & Farquharson 2015). However, the computational cost and memory requirements are large (Varilsuha and Candansayar, 2018) due to the direct solver of the large sparse matrix equation. This study proposes a new 3D MT modelling method in a mixed space-wavenumber domain based on equation 11. This simulation method mainly includes four steps starting from equation 11: (1) Utilize 2D Fourier transform along two horizontal directions; (2) Use the 1D finite element method to solve 1D differential equations with respect to the secondary EM potentials ($\mathbf{A}^s$, Φ^s) in the mixed space-wavenumber domain; (3) Iteratively update the electric field with a contraction operator until convergence; (4) Recover the EM fields and other parameters, such as the impedance tensor, in the spatial domain. To be specific, we transform x and y from the spatial domain into the wavenumber domain using Fourier transform regarding equation 11, then only the vertical direction, z, is preserved in the spatial domain. The 3D vector-scalar potential equations are simplified into 1D equations. The given 1D independent differential

equations can be computed in parallel among different wavenumbers, which improves the efficiency of 3D MT numerical simulation through parallelization. The finite element method is used to solve the 1D equations of the secondary EM potentials ($\mathbf{A}^s$, Φ^s) subjected to different wavenumbers. Meanwhile, a contraction operator based on the series expansion is used to iteratively update the secondary electric field until the field cannot be further updated. This is because the initial total electric field in equation 11 is calculated with a half space model, so that the primary field was used to represent the total field at the first iteration. Then, the iteration lasts until the secondary electric field cannot be further updated. After the calculation of the secondary electric field is done, the secondary magnetic field can be recovered through the corresponding potential $\mathbf{A}^s$. Finally, using inverse FFT we can add the secondary fields to the spatial primary EM fields to give the solution of 3D MT modelling in the spatial domain.

Governing equations in the mixed domain

By utilizing the Coulomb gauge condition, equation 11 can be written into sub-equations in the Cartesian coordinate system as

$$\begin{cases} \dfrac{\partial^2 A_x^s}{\partial x^2}+\dfrac{\partial^2 A_x^s}{\partial y^2}+\dfrac{\partial^2 A_x^s}{\partial z^2}+k_p^2 A_x^s-\mu_0\sigma^p\dfrac{\partial \Phi^s}{\partial x}=-\mu_0 j_x^s \\ \dfrac{\partial^2 A_y^s}{\partial x^2}+\dfrac{\partial^2 A_y^s}{\partial y^2}+\dfrac{\partial^2 A_y^s}{\partial z^2}+k_p^2 A_y^s-\mu_0\sigma^p\dfrac{\partial \Phi^s}{\partial y}=-\mu_0 j_y^s \\ \dfrac{\partial^2 A_z^s}{\partial x^2}+\dfrac{\partial^2 A_z^s}{\partial y^2}+\dfrac{\partial^2 A_z^s}{\partial z^2}+k_p^2 A_z^s-\mu_0\sigma^p\dfrac{\partial \Phi^s}{\partial z}=-\mu_0 j_z^s \\ \sigma^p\left(\dfrac{\partial^2 \Phi^s}{\partial x^2}+\dfrac{\partial^2 \Phi^s}{\partial y^2}+\dfrac{\partial^2 \Phi^s}{\partial z^2}\right)+\dfrac{\partial \Phi^s}{\partial z}\dfrac{\partial \sigma^p}{\partial z}-\mathrm{i}\omega A_z^s\dfrac{\partial \sigma^p}{\partial z} \\ \qquad\qquad =\dfrac{\partial j_x^s}{\partial x}+\dfrac{\partial j_y^s}{\partial y}+\dfrac{\partial j_z^s}{\partial z} \end{cases} . \tag{13}$$

Where, $j_x^s=\sigma^s E_x$, $j_y^s=\sigma^s E_y$ and $j_z^s=\sigma^s E_z$ are current density in three different

directions, respectively.

In two horizontal directions, we transform spatially related parameters into the wavenumber domain. Then, we obtain

$$\begin{cases} \dfrac{\partial^2 \tilde{A}_x^s}{\partial z^2} + \left(k_p^2 - k_x^2 - k_y^2\right)\tilde{A}_x^s + \mathrm{i}k_x\mu_0\tilde{\sigma}^p\tilde{\Phi}^s = -\mu_0\tilde{j}_x^s \\ \dfrac{\partial^2 \tilde{A}_y^s}{\partial z^2} + \left(k_p^2 - k_x^2 - k_y^2\right)\tilde{A}_y^s + \mathrm{i}k_y\mu_0\tilde{\sigma}^p\tilde{\Phi}^s = -\mu_0\tilde{j}_y^s \\ \dfrac{\partial^2 \tilde{A}_z^s}{\partial z^2} + \left(k_p^2 - k_x^2 - k_y^2\right)\tilde{A}_z^s - \tilde{\sigma}^p\mu_0\dfrac{\partial\tilde{\Phi}^s}{\partial z} = -\mu_0\tilde{j}_z^s \\ \left(\tilde{\sigma}^p\dfrac{\partial^2\tilde{\Phi}^s}{\partial z^2} + \dfrac{\partial\tilde{\sigma}^p}{\partial z}\dfrac{\partial\tilde{\Phi}^s}{\partial z} - \tilde{\sigma}^p\left(k_x^2 + k_y^2\right)\tilde{\Phi}^s\right) \\ \qquad -\mathrm{i}\omega\tilde{A}_z^s\dfrac{\partial\tilde{\sigma}^p}{\partial z} = -\mathrm{i}k_x\tilde{j}_x^s - \mathrm{i}k_y\tilde{j}_y^s + \dfrac{\partial\tilde{j}_z^s}{\partial z} \end{cases} . \tag{14}$$

Where, the symbol ~ marks parameters in a mixed space-wavenumber domain (Table 1), k_x and k_y are the wavenumbers in the mixed domain. Similar to 3D modelling of gravity and magnetic anomalies in a mixed space-wavenumber domain (Dai *et al*., 2019), equation 14 describes the vector-scalar potentials governing equations for 3D MT modelling with different wavenumbers in the mixed domain after 2D Fourier transform along the horizontal *x* and *y* directions. The selection of wavenumber with the Gauss-FFT method is based on the shift-sampling technique and Gaussian quadrature rule (Wu and Tian, 2014), and it can efficiently overcome the imposed periodicity and edge effect caused by FFT (Chai, 2009). Gauss-FFT with a two or four-node Gaussian quadrature rule has been proven to support a solution equivalent to a solution computed in the space domain (Wu and Tian 2014, Dai *et al.* 2019).

Through the above detailed formula derivation, a large-scale 3D complex EM equation system is transformed into a small-scale 1D simple EM equation system that is decoupled in horizontal wavenumber and amenable to fully parallel computation.

Thus, this 3D numerical modelling can be carried out on a multiple-core or a multiple-CPU computer with Open Multi-Processing (OpenMP). It is useful for large-scale EM surveys due to the reduction of memory demand. To solve equation 14, we have to iteratively update EM fields as the reason mentioned.

Boundary conditions

In a source-free region, the boundary conditions for the secondary EM potentials $(\tilde{\mathbf{A}}^s, \tilde{\Phi}^s)$ in the mixed space-wavenumber domain used in the modelling are shown as equations 15 and 16 (see more details in Appendix A),

$$\begin{cases} \dfrac{\partial \tilde{A}_x^s}{\partial z} = -s\tilde{A}_x^s + \dfrac{(t-s)}{\omega} k_x \tilde{\Phi}^s \\ \dfrac{\partial \tilde{A}_y^s}{\partial z} = -s\tilde{A}_y^s + \dfrac{(t-s)}{\omega} k_y \tilde{\Phi}^s \\ \dfrac{\partial \tilde{A}_z^s}{\partial z} = \mathrm{i}k_x \tilde{A}_x^s + \mathrm{i}k_y \tilde{A}_y^s \\ \dfrac{\partial \tilde{\Phi}^s}{\partial z} = -t\tilde{\Phi}^s \end{cases} \tag{15}$$

and

$$\begin{cases} \dfrac{\partial \tilde{A}_x^s}{\partial z} = s\tilde{A}_x^s - \mathrm{i}k_x \tilde{A}_z^s + \dfrac{sk_x \tilde{\Phi}^s}{\omega} \\ \dfrac{\partial \tilde{A}_y^s}{\partial z} = s\tilde{A}_y^s - \mathrm{i}k_y \tilde{A}_z^s + \dfrac{sk_y \tilde{\Phi}^s}{\omega} \\ \dfrac{\partial \tilde{A}_z^s}{\partial z} = \mathrm{i}k_x \tilde{A}_x^s + \mathrm{i}k_y \tilde{A}_y^s \\ \dfrac{\partial \tilde{\Phi}^s}{\partial z} = \mathrm{i}\omega \tilde{A}_z^s \end{cases}. \tag{16}$$

Where, $s^2 = k_x^2 + k_y^2 - k^2$ and $t^2 = k_x^2 + k_y^2$ are used for convenience. Since the Gauss-FFT method can efficiently overcome the imposed periodicity and edge effect. Therefore, the boundary conditions in the horizontal direction are automatically satisfied without extra consideration.

Finite element method

The finite element method with second-order interpolation (Xu, 1994; Jin, 2015) is an accurate approach to numerically solve the 1D governing equation in the mixed domain. Equations 14 – 16 are the 1D boundary value problems that the secondary EM potentials ($\tilde{\mathbf{A}}^s, \tilde{\Phi}^s$) satisfy. The mesh in vertical direction can increase with depth due to the diffusive nature of the EM fields, so that the accuracy and efficiency can be guaranteed simultaneously. With a chasing method (Temperton 1975, Boisvert 1991, Dai et al. 2019) it is possible to solve the matrix equation assembled by finite element analysis with a low cost even for a large-scale stiffness matrix.

The discrete finite element governing equations are derived with Galerkin's weighted residual method (Xu, 1994; Jin, 2015) in the mixed space-wavenumber domain, and the specific expressions are shown as (see more details in Appendix B)

$$
\begin{cases}
\sum_{e=1}^{Ne}\int_e\left(-\frac{\partial\tilde{A}_x^s}{\partial z}\frac{\partial N_i}{\partial z}+\left(k_p^2-k_x^2-k_y^2\right)N_i\,\tilde{A}_x^s+\mathrm{i}k_x\mu_0\tilde{\sigma}^pN_i\,\tilde{\Phi}^s+N_i\,\mu_0\tilde{j}_x^s\right)\mathrm{d}z \\
\qquad\qquad +\sum_{e=1}^{Ne}\int_s N_i\,\frac{\partial\tilde{A}_x^s}{\partial z}n_z\,\mathrm{d}z=0 \\
\sum_{e=1}^{Ne}\int_e\left(-\frac{\partial\tilde{A}_y^s}{\partial z}\frac{\partial N_i}{\partial z}+\left(k_p^2-k_x^2-k_y^2\right)N_i\,\tilde{A}_y^s+\mathrm{i}k_y\mu_0\tilde{\sigma}^pN_i\,\tilde{\Phi}^s+N_i\,\mu_0\tilde{j}_y^s\right)\mathrm{d}z \\
\qquad\qquad +\sum_{e=1}^{Ne}\int_s N_i\,\frac{\partial\tilde{A}_y^s}{\partial z}n_z\,\mathrm{d}z=0 \\
\sum_{e=1}^{Ne}\int_e\left(-\frac{\partial\tilde{A}_z^s}{\partial z}\frac{\partial N_i}{\partial z}+\left(k_p^2-k_x^2-k_y^2\right)N_i\,\tilde{A}_z^s-\mu_0\tilde{\sigma}^pN_i\,\frac{\partial\tilde{\Phi}^s}{\partial z}+N_i\,\mu_0\tilde{j}_z^s\right)\mathrm{d}z \\
\qquad\qquad +\sum_{e=1}^{Ne}\int_s N_i\,\frac{\partial\tilde{A}_z^s}{\partial z}n_z\,\mathrm{d}z=0 \\
\sum_{e=1}^{Ne}\int_e\left(-\tilde{\sigma}^p\frac{\partial\tilde{\Phi}^s}{\partial z}\frac{\partial N_i}{\partial z}+N_i\,\frac{\partial\tilde{\sigma}^p}{\partial z}\frac{\partial\tilde{\Phi}^s}{\partial z}-\tilde{\sigma}^p\left(k_x^2+k_y^2\right)N_i\,\tilde{\Phi}^s\right)\mathrm{d}z+ \\
\sum_{e=1}^{Ne}\int_e\left(-\mathrm{i}\omega N_i\,\frac{\partial\tilde{\sigma}^p}{\partial z}\tilde{A}_z^s+\mathrm{i}k_xN_i\,\tilde{j}_x^s+\mathrm{i}k_yN_i\,\tilde{j}_y^s-N_i\frac{\partial\tilde{j}_z^s}{\partial z}\right)\mathrm{d}z+ \\
\qquad\qquad \sum_{e=1}^{Ne}\int_s\tilde{\sigma}^pN_i\,\frac{\partial\tilde{\Phi}^s}{\partial z}n_z\,\mathrm{d}z=0
\end{cases}
. \qquad (17)
$$

Where, e represents the index of the elements, N_e is the number of the total elements, N_i represents the shape function, and n_z represents the normal vector. The mesh used in the study is structured.

In the z direction (Figure 1), a second-order shape function is utilized in the elements. As a result, the secondary vector potential $\tilde{\mathbf{A}}^s$ and the secondary scalar potential $\tilde{\Phi}^s$ have two values in each element along the z direction. Finally, a full stiffness matrix equation system is assembled by finite-element analysis as (see more details in Appendix C),

$$\mathbf{K}_{nz\times 4\times 23}\mathbf{u}_{nz\times 4} = \mathbf{P}_{nz\times 4}. \quad (18)$$

Where, the subscript nz is the number of vertical grid nodes, **u** is the unknown vector potential and scalar potential, **K** is a symmetric diagonal matrix with 23 rows regarding each cell, and **P** is a vector. The linear matrix equation to be solved is a fixed bandwidth system, and the chasing method selected is more efficient and convenient than solvers with preconditioners. Then, the secondary EM potentials ($\tilde{\mathbf{A}}^s, \tilde{\Phi}^s$) can be obtain in the mixed domain. Although we have to simultaneously solve the potentials at every node, however, the recovery of the fields in spatial domain only involves the observational locations and their neighbor nodes.

EM field components

Equations 3 and 4 can be decomposed into three sub-equations in the spatial domain, respectively,

281
$$\begin{cases} E_x = \mathrm{i}\omega A_x - \dfrac{\partial \Phi}{\partial x} \\ E_y = \mathrm{i}\omega A_y - \dfrac{\partial \Phi}{\partial y} \\ E_z = \mathrm{i}\omega A_z - \dfrac{\partial \Phi}{\partial z} \end{cases}, \tag{19}$$

282
$$\begin{cases} H_x = \dfrac{1}{\mu_0}\left(\dfrac{\partial A_z}{\partial y} - \dfrac{\partial A_y}{\partial z}\right) \\ H_y = \dfrac{1}{\mu_0}\left(\dfrac{\partial A_x}{\partial z} - \dfrac{\partial A_z}{\partial x}\right) \\ H_z = \dfrac{1}{\mu_0}\left(\dfrac{\partial A_y}{\partial x} - \dfrac{\partial A_x}{\partial y}\right) \end{cases}. \tag{20}$$

283 The utilization of the vector potential **A** and the electric potential Φ with the
284 Coulomb gauge renders clear physical meanings, which is shown in equations 19 and
285 20. The vector potential is associated with currents and accumulated charges at various
286 boundaries; however, the electric potential is only associated with accumulated charges.
287 If one applies our modelling strategy to ERT, the **E** fields would only have the electric
288 potential left in equation 19.

289 Using Fourier transform on equations 19 and 20 along two horizontal directions,
290 the secondary EM fields in the mixed space-wavenumber domain then satisfy the
291 following equations,

292
$$\begin{cases} \tilde{E}_x = i\omega\tilde{A}_x + ik_x\tilde{\Phi} \\ \tilde{E}_y = i\omega\tilde{A}_y + ik_y\tilde{\Phi} \\ \tilde{E}_z = i\omega\tilde{A}_z - \partial\tilde{\Phi}/\partial z \end{cases}, \tag{21}$$

293
$$\begin{cases} \tilde{H}_x = \dfrac{1}{\mu_0}\left(-\mathrm{i}k_y\tilde{A}_z - \dfrac{\partial\tilde{A}_y}{\partial z}\right) \\ \tilde{H}_y = \dfrac{1}{\mu_0}\left(\dfrac{\partial\tilde{A}_x}{\partial z} + \mathrm{i}k_x\tilde{A}_z\right) \\ \tilde{H}_z = \dfrac{1}{\mu_0}\left(-\mathrm{i}k_x\tilde{A}_y + \mathrm{i}k_y\tilde{A}_x\right) \end{cases}. \tag{22}$$

294 $\partial\tilde{\Phi}/\partial z$, $\partial\tilde{A}_x/\partial z$ and $\partial\tilde{A}_y/\partial z$ can be obtained using the method of Jin (2015). When

295 equation 18 is solved, the secondary vector potential $\tilde{\mathbf{A}}^{s}$ and the secondary scalar
296 potential $\tilde{\Phi}^{s}$ and their derivatives can be used to calculate the secondary EM fields.
297 Afterwards, 2D inverse Fourier transform is used to recover the fields in spatial domain
298 (Tontini et al., 2009; Wu and Tian, 2014). With addition of the primary field, the total
299 EM fields and impedance tensor can be calculated.

300 **Electric field iteration in the spatial domain**

301 The primary electric field rather than total electric field is used to solve equation
302 11 for the first step, then an approach similar to the Born approximation is utilized to
303 iteratively reduce the inaccuracy of the secondary electric field solved by 1D FEM in
304 the mixed domain. In order to achieve a stable and accurate solution for the EM fields,
305 an iterative method utilized in the integral equation is adopted to update the secondary
306 electric field and then the total field, until the total **E** field cannot be further updated.

307 Based on the Green's function of electric field, the electric field integral equation
308 can be written as (Avdeev et al., 1997; Hursán and Zhdanov, 2002)

309
$$\mathbf{E}\left(\mathbf{r}_j\right)=\mathbf{E}^{\mathrm{p}}\left(\mathbf{r}_j\right)+G\left[\Delta\sigma\left(\mathbf{r}\right)\cdot\mathbf{E}\left(\mathbf{r}\right)\right], \tag{23}$$

310 where, **E** is the total field, $\mathbf{E}^{\mathrm{p}}$ is the primary field, $\Delta\sigma$ is abnormal conductivity, $\mathbf{r}_j$
311 and $\mathbf{r}$ represent receiver position and anomaly position, respectively, and $G(\cdot)$ is a
312 linear operator of

313
$$G(\cdot)=\iiint_{\mathrm{V}}\bar{\mathbf{G}}\left(\mathbf{r},\mathbf{r}'\right)\mathrm{dv}. \tag{24}$$

314 Where, $\bar{\mathbf{G}}\left(\mathbf{r},\mathbf{r}'\right)$ is the Green's function of electric field.

315 The iterative method can be used to solve equation 23 in the form of

316
$$\mathbf{E}^{(n)}=\mathbf{E}^{\mathrm{p}}+G\left[\Delta\sigma\cdot\mathbf{E}^{(n-1)}\right]. \tag{25}$$

The Banach theorem (Gao, 2005) in functional analysis shows that the convergence condition for equation 25 is

$$\left\| G\left(\Delta\sigma \cdot \left(\mathbf{E}^{(n-1)} - \mathbf{E}^{(n)} \right) \right) \right\| < \kappa \left\| \Delta\sigma \cdot \left(\mathbf{E}^{(n-1)} - \mathbf{E}^{(n)} \right) \right\|. \tag{26}$$

Where, the iterative coefficient $\kappa < 1$ is required，and $\|\cdot\|$ represents L_2 norm. Thus, the condition that satisfies the above equation is

$$\|G\| < 1. \tag{27}$$

The operator G, with contraction feature, is modified based on the energy inequality (Gao, 2005; Hursán and Zhdanov, 2002), and then the following iterative scheme is constructed to satisfy the requirement of the operator G,

$$\mathbf{E}^{(n)} = \alpha \mathbf{E}^{(n)} + \beta \mathbf{E}^{(n-1)}. \tag{28}$$

Where

$$\alpha = \frac{2\sigma^p}{2\sigma^p + \Delta\sigma}, \tag{29}$$

$$\beta = \frac{\Delta\sigma}{2\sigma^p + \Delta\sigma}, \tag{30}$$

where σ^p represents background conductivity, $\Delta\sigma$ represents the anomalous conductivity. $\mathbf{E}^{(n)}$ represents the secondary electric field calculated with equation 21 in addition with the primary electric field, and $\mathbf{E}^{(n-1)}$ represents value from previous iteration (set as 0 for the first iteration). The iterative relationship is used to update the right-hand side of equation 11 to approximate an accurate solution. After the FE solution, we recovered the total field **E** in the spatial domain, then updated the total field **E** with equation 28. The updated **E**-field is transformed into the Fourier domain before the FE matrix is solved again.

RESULTS

Model 1: Comparison with IE algorithm

The cuboid model shown in Figure 1 is used to evaluate the accuracy of 3D MT modelling. The proposed algorithm can be implemented with either the Gauss FFT method or the standard FFT method with grid expansion (Dai et al., 2019). As previously studied (see details in Dai et al. 2019), the Gauss FFT and the standard FFT both have advantages and disadvantages with respect to accuracy and efficiency. Particularly, when the model is discretized into a large number of elements, the standard FFT method with sufficient grid expansion is a good option, otherwise, the Gauss FFT method is a preferred option. The grid expansion requires several attempts to set up the expansion area to guarantee the accuracy. However, it is not straightforward to model field data with different tests of the grid expansion; the Gauss FFT is utilized in this study.

The model region is $2\times2\times0.7$ km^3 and discretized into $51\times51\times75$ nodes. However, the first two numbers, 51×51, represent the number of wavenumbers (the same as other examples). It contains 10 grid-points in the vertical direction in the air layer. The frequencies selected are 0.01, 0.1, 1, and 10 Hz. The volume of a conductive anomaly is $0.8\times0.4\times0.4$ km^3, and the top of the anomaly is located at 0.2 km depth. The resistivities of the homogeneous half-space, the anomaly, and the air are 100, 10, and 10^8 Ωm, respectively.

The new approach combined with the iterative scheme is applied to compute the EM fields. The machine used for calculation has 4 Intel(R) i7 Cores with 2.60 GHz

main frequency and 8 GB memory. The programming language is Fortran, and the Fortran code is parallelized with OpenMP.

To verify the accuracy of the final solution, the calculated responses of the designed model are compared with responses of the IE solution given by Hursán & Zhdanov (2002). The variation of iteration fitting errors against iteration number is shown in Figure 2. The fitting errors of *XY* mode (*x* direction polarization) and *YX* mode (*y* direction polarization) are less than 0.1% after ten iterations, and the convergence of *YX* mode is more stable than *XY* mode due to the non-centrosymmetry of the cuboid anomaly. The simulation in this study iterates 15 times in total. The responses at 10 Hz obtained from the proposed algorithm using the Gauss FFT method with the four-node Gaussian quadrature rule are compared with the responses of the IE algorithm in detail (Figure 3). Their relative differences of $|V_{new} - V_{IE}|/ V_{IE}$ on the plane of z = 0 are also shown (Figure 3). The response differences between the two methods are less than 0.6 % (Figure 3), which is generally smaller than the error floor of field data. Moreover, the phase data have even smaller relative differences than the apparent resistivity data. The relative differences of apparent resistivities and phases along a selected profile, marked as red line in Figure 1, are shown in Figure 4. The responses of the four different frequencies are compared with each other. The relative differences of apparent resistivity and phase for 0.01, 0.1, and 1 Hz frequency are smaller than the differences for 10 Hz (Figures 4a-d). Again, the relative differences in the phases are smaller than the relative differences in apparent resistivities. Therefore, the accuracy of the proposed algorithm is reasonable. The computation time for the *XY* mode and *YX* mode at 10 Hz

382 is 44 s using the proposed method. However, the executable code of the IE algorithm is
383 run with MATLAB, which can slow down the efficiency of the IE algorithm. So that,
384 the calculation time of the IE algorithm is not further analyzed. Instead, the calculation
385 efficiency is studied in the following examples by comparing our algorithm with other
386 FEM algorithms (Ren et al., 2013; Jahandari and Farquharson, 2017).

387 **Model 2: Comparison with an adaptive FEM algorithm**

388 A 3D model modified after Zhdanov et al. (2006) is used to further evaluate the 3D
389 MT modelling accuracy. The model region is discretized into 101×101×71 nodes
390 including 10 grid-points in the vertical direction in the air layer (Figure 5). The
391 frequency tested is 0.1 Hz. Two anomalies, one conductor and one resistor, are buried
392 in a half-space model. The volume of each anomaly is $0.4\times0.4\times0.4$ km^3, and the top of
393 the anomaly is located at 0.2 km depth (Figure 5). The resistivities of the homogeneous
394 half-space, the conductive anomaly, the resistive anomaly, and the air are 100, 10, 1000,
395 and 10^8 Ωm, respectively.

396 The solution of our method is compared with the adaptive FEM solution given by
397 Ren et al. (2013) based on the same anomaly settings. The responses at 0.1 Hz
398 calculated using the Gauss FFT method with the four-node Gaussian quadrature rule
399 are plotted together with the responses at the same frequency from the adaptive FEM
400 algorithm (Figure 6). The proposed algorithm iterates 15 times in total. The reference
401 algorithm also iterates 15 times. However, the purposes of the iterations are different in
402 the two algorithms. The former is due to the inaccurate total **E** field used to solve
403 equation 11; the latter is due to the refinement of the FE grids. Since the algorithm of

Ren et al. (2013) has been well tested, the results of the algorithm are treated as a reference solution. Clearly, the two results are very similar to each other (Figures 6a-6d). The relative differences of the two results, $(V_{new} - V_{FEM})/V_{FEM}$, on the plane of z = 0 are shown in Figures 6e-6h. The relative differences are in general within 5 % except at a few data points, which is smaller than the typical error floor of MT field data. Moreover, the phase data show smaller relative differences than the apparent resistivity data. Therefore, the accuracy of the proposed algorithm is reasonable.

The calculation time of our method is 143 s, which is 1199 s less than the calculation time of the adaptive FEM after 15 iterations in total. However, the calculation time for the 15th iteration of the adaptive FEM is only 151 s, which is slightly slower than the time required by our method. One should note that, without the previous 14 iterations, the final optimal mesh at the 15th iteration would not be easy to obtain. The maximum memory usage of our algorithm is 0.44 GB, which is 7 GB less than the one used for the adaptive FEM at the 15th iteration. The calculations were performed with 4 cores and two anomalies were introduced in the model, that is why the calculation time with Ren et al. (2013) is longer than the time in the original publication. By analyzing the calculation time for this two-anomaly model and a one-anomaly model with our method and the adaptive FEM of Ren et al. (2013) respectively, we can estimate that about 70 % of the increased calculation time is caused by the increased model complexity.

One advantage of the proposed algorithm is that large padding to account for boundary conditions is unnecessary. In this case, our model size is only 2×2×1.4 km^3.

426 This is because all the horizontal information of the proposed algorithm is in Fourier
427 domain and the Gauss FFT can remove the edge effect implicitly. In contrast, the model
428 used by Ren et al. (2013) expanded the model region to 140×140×140 km^3. Even
429 though 322,620 elements were used in the algorithm of Ren et al. (2013) after 15
430 iterations due to the efficiency of the adaptive FEM, a larger number of elements are
431 needed by using other FE methods to discretize such a model. However, the proposed
432 algorithm transforms the 3D problem into 1D problems to reduce memory demand and
433 even has a higher efficiency than the algorithm of Ren et al. (2013).

434 **Model 3: Comparison with a non-adaptive FEM algorithm**

435 In order to further test the computational efficiency advantage of this algorithm, a
436 large mesh is designed for a 3D model with a quasi-spherical anomaly (Figure 7). The
437 model is discretized into 251×251×151 nodes and occupies a region of 5×5×3 km^3. A
438 resistive spherical anomaly, 1000 Ωm, with a radius of 0.4 km is buried at 1.4 km depth
439 (Figure 7). Surrounding of the sphere is a 100 Ωm half space. We compare the algorithm
440 with the one of Jahandari and Farquharson (2017), which uses an edge-based FEM but
441 with tetrahedral elements. After careful tests, 6.98 million elements are required for the
442 algorithm of Jahandari and Farquharson (2017) to provide an accurate modelling result
443 at the observational locations (251×251) in this example. With the goal-oriented
444 adaptive FEM algorithm (Ren et al., 2013), the number of elements in the final iteration
445 should be smaller than the algorithm of Jahandari and Farquharson (2017). However,
446 the price of generating such efficient discretization is to iterate the modelling, which is
447 not avoidable with goal-oriented adaptive FEM.

448 The responses at 1 Hz were modelled with the proposed algorithm using the Gauss
449 FFT method with the two-node Gaussian quadrature rule and with the algorithm of
450 Jahandari and Farquharson (2017), respectively. The responses cannot be further
451 improved after 11 iterations for the proposed method, and no iteration is required for
452 the algorithm of Jahandari and Farquharson (2017). The apparent resistivities and
453 phases at ground level show a resistor beneath the observational surface (Figure 8).
454 Because the MT data are not sensitive to resistors, the maximum apparent resistivity of
455 ρ_{xy} and ρ_{yx} is only 103 Ωm in both results. The spatial FE results are not completely
456 symmetric due to the unstructured mesh generation with Tetgen (Si, 2015). Also,
457 rectilinear grids generally result in smoother patterns in the data. However, the relative
458 differences, $|V_{new} - V_{FEM}|/V_{FEM}$, of the two results are small in Figure 8 (< 0.4 % in
459 both apparent resistivities and phases). Even though the anomaly is approximately
460 spherical, the example shows the potential of our method to handle complex 3D models
461 with a fine discretization.
462 This example also demonstrates the efficiency advantages of the proposed method.
463 With the proposed method, single-frequency EM fields for 251×251 observation points
464 were computed using the Gauss FFT method in 1858 s with only 4 cores, and the largest
465 memory requirement in the entire calculation is 4.9 GB. However, with the usage of
466 MUMPS, the algorithm of Jahandari and Farquharson (2017) requires 25,750 s
467 computation time and 202 GB memory in total for 4 Intel(R) Xeon cores with 2.2 GHz
468 main frequency. Hence, our proposed algorithm can quickly compute the EM fields for
469 large-scale models in comparison with the algorithm of Jahandari and Farquharson

(2017) and can promisingly be used for the 3D MT inversion problem based on either deterministic schemes or probabilistic schemes, such as the Bayesian method with a realistic model. The larger the meshing scale, the more obvious the computational efficiency of the algorithm for the 3D MT numerical simulation (highly speculated the same for ERT and CSEM methods). Additionally, if the standard FFT with grid expansion is used rather than the Gauss FFT, the calculation efficiency can be further improved (Dai et al., 2019). However, grid expansion requires several attempts to set up a sufficient expansion area to guarantee the accuracy.

CONCLUSIONS

A new 3D MT modelling algorithm in a mixed space-wavenumber domain is implemented and presented in this study. The accuracy and efficiency of the newly proposed method are verified with three synthetic 3D models by the comparison with a classical IE solution and two well-tested FEM solutions.

The algorithm that transforms the 3D spatial partial differential equations of the vector-scalar potentials into 1D equations using Fourier transform along horizontal directions can give sufficient accuracy and substantial computational advantages over other published modelling methods. Our method mitigates the memory requirement for about 94 % and 75% in the second and third synthetic tests, respectively. This indicates that the more complexity a model has, the more memory requirement reduction the method provides. The finite element method together with the chasing method can solve the 1D vector-scalar potential equations containing different wavenumbers, and the simulation efficiency is improved due to the parallelism among different wavenumbers

and the dimensionality reduction. The new algorithm is about 8-12 times faster than other FEM algorithms, suggesting our method is a good candidate for the Bayesian inversion. Since the primary-secondary field separation strategy is applied in our method, extra consideration is needed for including topography, such as calculating the responses of topography numerically. It is worth mentioning that the method can also be used for ERT and CSEM 3D modelling with source inclusion.

ACKNOWLEDGEMENTS

The study was supported by the Natural Science Foundation of China (grant no. 41574127) and the Natural Science Foundation of Guangxi Province (grant no. GXNSFGA380004). S.W. was funded by the Norwegian Research Council together with the industry partners of the GAMES consortium and the Centre of Geophysical Forecasting at Norwegian University of Science and Technology (grant no. 294404, 309960, and 324442). Partial computations were performed on resources provided by Sigma2 - the National Infrastructure for High Performance Computing and Data Storage in Norway. We appreciate C.G. Farquharson and two anonymous reviewers for their constructive comments. The associate editor X. Hu and the editor J. Etgen are also appreciated for their suggestions to improve this article. The data are available under request.

APPENDIX A: BOUNDARY CONDITIONS

In a homogeneous medium, the EM fields satisfy the following Helmholtz equation

$$\frac{\partial^2 \mathbf{E}^s}{\partial x^2}+\frac{\partial^2 \mathbf{E}^s}{\partial y^2}+\frac{\partial^2 \mathbf{E}^s}{\partial z^2}+k^2\mathbf{E}^s=0. \tag{A1}$$

The 2D Fourier transform in x and y directions is used to express equation A1 into the mixed space-wavenumber domain, then we obtain

$$\frac{\partial^2 \tilde{\mathbf{E}}^s}{\partial z^2}-s^2\tilde{\mathbf{E}}^s=0. \tag{A2}$$

Where， $s^2=k_x^2+k_y^2-k^2$ will be used for compactness of notation. There is only a downward traveling wave at the lower boundary based on the propagation law of electromagnetic waves,

$$\frac{\partial \tilde{\mathbf{E}}^s}{\partial z}=-s\tilde{\mathbf{E}}^s. \tag{A3}$$

Equations A3 can be written into the sub-equation form

$$\begin{cases}\dfrac{\partial \tilde{E}_x^s}{\partial z}=-s\tilde{E}_x^s\\ \dfrac{\partial \tilde{E}_y^s}{\partial z}=-s\tilde{E}_y^s\end{cases}. \tag{A4}$$

Meanwhile, applying the 2D Fourier transform to equation 4, we obtain

$$\begin{cases}\tilde{E}_x^s=\mathrm{i}\omega\tilde{A}_x^s+\mathrm{i}k_x\tilde{\Phi}^s\\ \tilde{E}_y^s=\mathrm{i}\omega\tilde{A}_y^s+\mathrm{i}k_y\tilde{\Phi}^s\\ \tilde{E}_z^s=\mathrm{i}\omega\tilde{A}_z^s-\partial\tilde{\Phi}^s/\partial z\end{cases}. \tag{A5}$$

Through replacing the electric field with $\tilde{E}_x^s$ and $\tilde{E}_y^s$ in equation A5, equation A4 can be rewritten as

$$\begin{cases} \dfrac{\partial \tilde{A}_x^s}{\partial z} = -s\tilde{A}_x^s - \dfrac{sk_x\tilde{\Phi}^s}{\omega} - \dfrac{k_x}{\omega}\dfrac{\partial \tilde{\Phi}^s}{\partial z} \\ \dfrac{\partial \tilde{A}_y^s}{\partial z} = -s\tilde{A}_y^s - \dfrac{sk_y\tilde{\Phi}^s}{\omega} - \dfrac{k_y}{\omega}\dfrac{\partial \tilde{\Phi}^s}{\partial z} \end{cases}. \tag{A6}$$

Similarly, applying the 2D Fourier transform to the Coulomb-gauge formulation $\nabla \cdot \mathbf{A} = 0$, we obtain

$$\frac{\partial \tilde{A}_z^s}{\partial z} = \mathrm{i}k_x\tilde{A}_x^s + \mathrm{i}k_y\tilde{A}_y^s. \tag{A7}$$

In a homogeneous medium, the scalar potential (Φ) satisfies the following equation

$$\frac{\partial^2\Phi^s}{\partial x^2} + \frac{\partial^2\Phi^s}{\partial y^2} + \frac{\partial^2\Phi^s}{\partial z^2} = 0. \tag{A8}$$

Meanwhile, applying the 2D Fourier transform to equation A8, we obtain

$$\frac{\partial^2\tilde{\Phi}^s}{\partial z^2} - t^2\tilde{\Phi}^s = 0. \tag{A9}$$

Where $t^2 = k_x^2 + k_y^2$ is used for convenience. Similarly, the lower boundary conditions of the scalar potential in a mixed space-wavenumber domain can be obtained

$$\frac{\partial \tilde{\Phi}^s}{\partial z} = -t\tilde{\Phi}^s. \tag{A10}$$

The lower boundary conditions used in the modelling approach can be described as,

$$\begin{cases} \dfrac{\partial \tilde{A}_x^s}{\partial z} = -s\tilde{A}_x^s + \dfrac{(t-s)}{\omega}k_x\tilde{\Phi}^s \\ \dfrac{\partial \tilde{A}_y^s}{\partial z} = -s\tilde{A}_y^s + \dfrac{(t-s)}{\omega}k_y\tilde{\Phi}^s \\ \dfrac{\partial \tilde{A}_z^s}{\partial z} = \mathrm{i}k_x\tilde{A}_x^s + \mathrm{i}k_y\tilde{A}_y^s \\ \dfrac{\partial \tilde{\Phi}^s}{\partial z} = -t\tilde{\Phi}^s \end{cases}. \tag{A11}$$

The upper boundary conditions can be obtained by the same derivation method

$$\begin{cases} \dfrac{\partial \tilde{A}_x^s}{\partial z} = s\tilde{A}_x^s - \mathrm{i}k_x\tilde{A}_z^s + \dfrac{sk_x\tilde{\Phi}^s}{\omega} \\ \dfrac{\partial \tilde{A}_y^s}{\partial z} = s\tilde{A}_y^s - \mathrm{i}k_y\tilde{A}_z^s + \dfrac{sk_y\tilde{\Phi}^s}{\omega} \\ \dfrac{\partial \tilde{A}_z^s}{\partial z} = \mathrm{i}k_x\tilde{A}_x^s + \mathrm{i}k_y\tilde{A}_y^s \\ \dfrac{\partial \tilde{\Phi}^s}{\partial z} = \mathrm{i}\omega\tilde{A}_z^s \end{cases}. \tag{A14}$$

APPENDIX B: THE EQUIVALENCE BETWEEN VARIATIONAL PROBLEM AND BOUNDARY VALUE PROBLEM

The Galerkin method is used on the vector potential ($\tilde{\mathbf{A}}$) and scalar potential ($\tilde{\Phi}$) system of equations (Xu, 1994; Jin, 2015), and we can obtain the margin equation

$$\begin{cases} R_{e1}=\dfrac{\partial^2\tilde{A}_x^s}{\partial z^2}+\left(k_p^2-k_x^2-k_y^2\right)\tilde{A}_x^s+\mathrm{i}k_x\mu_0\tilde{\sigma}^p\tilde{\Phi}^s+\mu_0\tilde{j}_x^s \\ R_{e2}=\dfrac{\partial^2\tilde{A}_y^s}{\partial z^2}+\left(k_p^2-k_x^2-k_y^2\right)\tilde{A}_y^s+\mathrm{i}k_y\mu_0\tilde{\sigma}^p\tilde{\Phi}^s+\mu_0\tilde{j}_y^s \\ R_{e3}=\dfrac{\partial^2\tilde{A}_z^s}{\partial z^2}+\left(k_p^2-k_x^2-k_y^2\right)\tilde{A}_z^s-\tilde{\sigma}^p\mu_0\dfrac{\partial\tilde{\Phi}^s}{\partial z}+\mu_0\tilde{j}_z^s \\ R_{e4}=\left(\tilde{\sigma}^p\dfrac{\partial^2\tilde{\Phi}^s}{\partial z^2}+\dfrac{\partial\tilde{\sigma}^p}{\partial z}\dfrac{\partial\tilde{\Phi}^s}{\partial z}-\tilde{\sigma}^p\left(k_x^2+k_y^2\right)\tilde{\Phi}^s\right) \\ \qquad\qquad -\mathrm{i}\omega\tilde{A}_z^s\dfrac{\partial\tilde{\sigma}^p}{\partial z}+\mathrm{i}k_xj_x^s+\mathrm{i}k_yj_y^s-\dfrac{\partial\tilde{j}_z^s}{\partial z} \end{cases}. \tag{B1}$$

Letting the weighted integral of equation B1 in the whole integral region be zero, we obtain

$$\begin{cases} \int_\Omega N_i\,R_{e1}\,\mathrm{d}z=\sum_{e=1}^{Ne}\int_e N_i\,R_{e1}\,\mathrm{d}z=0 \\ \int_\Omega N_i\,R_{e2}\,\mathrm{d}z=\sum_{e=1}^{Ne}\int_e N_i\,R_{e2}\,\mathrm{d}z=0 \\ \int_\Omega N_i\,R_{e3}\,\mathrm{d}z=\sum_{e=1}^{Ne}\int_e N_i\,R_{e3}\,\mathrm{d}z=0 \\ \int_\Omega N_i\,R_{e4}\,\mathrm{d}z=\sum_{e=1}^{Ne}\int_e N_i\,R_{e4}\,\mathrm{d}z=0 \end{cases}. \tag{B2}$$

Where Ω is integral area, Ne is the number of vertical elements, $N_i\ (i=j,p,m)$ is the second-order interpolation function, and the specific expressions can be described as (Xu, 1994)

$$N_j=\left(2L_j-1\right)L_j,\quad N_p=4L_jL_m,\quad N_m=\left(2L_m-1\right)L_m, \tag{B3}$$

and,

$$L_j(z)=\frac{z_m-z}{z_m-z_j}=\frac{l_j}{l},\ L_m(z)=\frac{z-z_j}{z_m-z_j}=\frac{l_m}{l}. \tag{B4}$$

Here z_j and z_m are the global coordinate in the vertical direction under the Cartesian coordinate system (Figure B1).

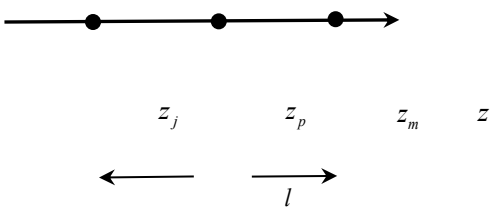

Figure B1. Length scheme.

Substituting margin equation B1 into equation B2, we obtain

$$\begin{cases}
\sum_{e=1}^{Ne}\int_e N_i\left(\frac{\partial^2\tilde{A}_x^s}{\partial z^2}+\left(k_p^2-k_x^2-k_y^2\right)\tilde{A}_x^s+\mathrm{i}k_x\mu_0\tilde{\sigma}^p\tilde{\Phi}^s+\mu_0\tilde{j}_x^s\right)\mathrm{dz}=0\\
\sum_{e=1}^{Ne}\int_e N_i\left(\frac{\partial^2\tilde{A}_y^s}{\partial z^2}+\left(k_p^2-k_x^2-k_y^2\right)\tilde{A}_y^s+\mathrm{i}k_y\mu_0\tilde{\sigma}^p\tilde{\Phi}^s+\mu_0\tilde{j}_y^s\right)\mathrm{dz}=0\\
\sum_{e=1}^{Ne}\int_e N_i\left(\frac{\partial^2\tilde{A}_z^s}{\partial z^2}+\left(k_p^2-k_x^2-k_y^2\right)\tilde{A}_z^s-\tilde{\sigma}^p\mu_0\frac{\partial\tilde{\Phi}^s}{\partial z}+\mu_0\tilde{j}_z^s\right)\mathrm{dz}=0\\
\sum_{e=1}^{Ne}\int_e\left(N_i\left(\tilde{\sigma}^p\frac{\partial^2\tilde{\Phi}^s}{\partial z^2}+\frac{\partial\tilde{\sigma}^p}{\partial z}\frac{\partial\tilde{\Phi}^s}{\partial z}-\tilde{\sigma}^p\left(k_x^2+k_y^2\right)\tilde{\Phi}^s\right)\mathrm{dz}\right)+\\
\qquad\sum_{e=1}^{Ne}\int_e N_i\left(-\mathrm{i}\omega\tilde{A}_z^s\frac{\partial\tilde{\sigma}^p}{\partial z}\right)+N_i\left(\mathrm{i}k_xj_x^s+\mathrm{i}k_yj_y^s-\frac{\partial\tilde{j}_z^s}{\partial z}\right)\mathrm{dz}=0
\end{cases}. \tag{B5}$$

The Green's integral formula can be written as

$$\int_e \phi\frac{\partial\varphi}{\partial z}\mathrm{dz}=-\int_e \varphi\frac{\partial\phi}{\partial z}\mathrm{dz}+\oint_{\partial e}\varphi\phi n_z\mathrm{dl}. \tag{B6}$$

Using Green's formula B6 to reduce each term of equation B5, we obtain

$$\begin{cases}
\int_e N_i\frac{\partial^2\tilde{A}_x^s}{\partial z^2}\mathrm{dz}=-\int_e\frac{\partial\tilde{A}_x^s}{\partial z}\frac{\partial N_i}{\partial z}\mathrm{dz}+\int_s N_i\frac{\partial\tilde{A}_x^s}{\partial z}n_z\,\mathrm{dz}\\
\int_e N_i\frac{\partial^2\tilde{A}_y^s}{\partial z^2}\mathrm{dz}=-\int_e\frac{\partial\tilde{A}_y^s}{\partial z}\frac{\partial N_i}{\partial z}\mathrm{dz}+\int_s N_i\frac{\partial\tilde{A}_y^s}{\partial z}n_z\,\mathrm{dz}\\
\int_e N_i\frac{\partial^2\tilde{A}_z^s}{\partial z^2}\mathrm{dz}=-\int_e\frac{\partial\tilde{A}_z^s}{\partial z}\frac{\partial N_i}{\partial z}\mathrm{dz}+\int_s N_i\frac{\partial\tilde{A}_z^s}{\partial z}n_z\,\mathrm{dz}\\
\int_e N_i\frac{\partial\tilde{\sigma}^p}{\partial z}\frac{\partial\tilde{\Phi}^s}{\partial z}\mathrm{dz}=-\int_e\tilde{\sigma}^p\frac{\partial\tilde{\Phi}^s}{\partial z}\frac{\partial N_i}{\partial z}\mathrm{dz}+\int_s\tilde{\sigma}^p\frac{\partial\tilde{\Phi}^s}{\partial z}N_i\,n_z\,\mathrm{dz}
\end{cases}. \tag{B7}$$

575 Therefore, the final coupled equations required to be solved are

$$
\begin{cases}
\sum_{e=1}^{Ne}\int_e\left(-\frac{\partial\tilde{A}_x^s}{\partial z}\frac{\partial N_i}{\partial z}+\left(k_p^2-k_x^2-k_y^2\right)N_i\,\tilde{A}_x^s+\mathrm{i}\,k_x\mu_0\tilde{\sigma}^p N_i\,\tilde{\Phi}^s+N_i\,\mu_0\tilde{j}_x^s\right)\mathrm{dz} \\
\qquad\qquad +\sum_{e=1}^{Ne}\int_s N_i\,\frac{\partial\tilde{A}_x^s}{\partial z}n_z\,\mathrm{dz}=0 \\
\sum_{e=1}^{Ne}\int_e\left(-\frac{\partial\tilde{A}_y^s}{\partial z}\frac{\partial N_i}{\partial z}+\left(k_p^2-k_x^2-k_y^2\right)N_i\,\tilde{A}_y^s+\mathrm{i}\,k_y\mu_0\tilde{\sigma}^p N_i\,\tilde{\Phi}^s+N_i\,\mu_0\tilde{j}_y^s\right)\mathrm{dz} \\
\qquad\qquad +\sum_{e=1}^{Ne}\int_s N_i\,\frac{\partial\tilde{A}_y^s}{\partial z}n_z\,\mathrm{dz}=0 \\
\sum_{e=1}^{Ne}\int_e\left(-\frac{\partial\tilde{A}_z^s}{\partial z}\frac{\partial N_i}{\partial z}+\left(k_p^2-k_x^2-k_y^2\right)N_i\,\tilde{A}_z^s-\mu_0\tilde{\sigma}^p N_i\,\frac{\partial\tilde{\Phi}^s}{\partial z}+N_i\,\mu_0\tilde{j}_z^s\right)\mathrm{dz} \\
\qquad\qquad +\sum_{e=1}^{Ne}\int_s N_i\,\frac{\partial\tilde{A}_z^s}{\partial z}n_z\,\mathrm{dz}=0 \\
\sum_{e=1}^{Ne}\int_e\left(-\tilde{\sigma}^p\frac{\partial\tilde{\Phi}^s}{\partial z}\frac{\partial N_i}{\partial z}+N_i\,\frac{\partial\tilde{\sigma}^p}{\partial z}\frac{\partial\tilde{\Phi}^s}{\partial z}-\tilde{\sigma}^p\left(k_x^2+k_y^2\right)N_i\,\tilde{\Phi}^s\right)\mathrm{dz}+ \\
\sum_{e=1}^{Ne}\int_e\left(-\mathrm{i}\,\omega N_i\,\frac{\partial\tilde{\sigma}^p}{\partial z}\tilde{A}_z^s+\mathrm{i}\,k_x N_i\,\tilde{j}_x^s+\mathrm{i}\,k_y N_i\,\tilde{j}_y^s-N_i\frac{\partial\tilde{j}_z^s}{\partial z}\right)\mathrm{dz}+ \\
\qquad\qquad \sum_{e=1}^{Ne}\int_s\tilde{\sigma}^p N_i\,\frac{\partial\tilde{\Phi}^s}{\partial z}n_z\,\mathrm{dz}=0
\end{cases}
\tag{B8}
$$

577

APPENDIX C: FINITE ELEMENT ANALYSIS

The vector and scalar potentials in equation 17 are expressed as a second-order interpolation function,

$$\begin{cases} \tilde{\Phi}^s = \sum_{i=1}^{3} N_i \tilde{\Phi}_i^s \\ \tilde{A}_x^s = \sum_{i=1}^{3} N_i \tilde{A}_{xi}^s \\ \tilde{A}_y^s = \sum_{i=1}^{3} N_i \tilde{A}_{yi}^s \\ \tilde{A}_z^s = \sum_{i=1}^{3} N_i \tilde{A}_{zi}^s \\ \hat{y}_p = \sum_{i=1}^{3} N_i \hat{y}_{pi} \\ \tilde{j}_z^s = \sum_{i=1}^{3} N_i \tilde{j}_{zi} \end{cases} \quad i = 1,2,3. \tag{C1}$$

Substituting equation C1 into equation 17, and equation 18 can be formed by finite element analysis. The following seven types of integral cover all integral types of equation 17, and other integral terms can be found in these seven types of integral.

1) The first element integral form in equation 17 is

$$\int_e \frac{\partial \tilde{A}_x^s}{\partial z} \frac{\partial N_i}{\partial z} \mathrm{d}z = \mathbf{K_{1e}} \tilde{A}_{xe}^s = \frac{1}{3l} \begin{pmatrix} 7 & -8 & 1 \\ -8 & 16 & -8 \\ 1 & -8 & 7 \end{pmatrix} \begin{pmatrix} \tilde{A}_{xj}^s \\ \tilde{A}_{xp}^s \\ \tilde{A}_{xm}^s \end{pmatrix}. \tag{C2}$$

2) The second element integral form in equation 17 is

$$\int_e N_i \tilde{A}_x^s \, \mathrm{d}z = \mathbf{K_{2e}} \tilde{A}_{xe}^s = \frac{l}{30} \begin{pmatrix} 4 & 2 & -1 \\ 2 & 16 & 2 \\ -1 & 2 & 4 \end{pmatrix} \begin{pmatrix} \tilde{A}_{xj}^s \\ \tilde{A}_{xp}^s \\ \tilde{A}_{xm}^s \end{pmatrix}. \tag{C3}$$

3) The third element integral form in equation 17 is

$$\int_e N_i \frac{\partial \tilde{A}_x^s}{\partial z} dz = \mathbf{K_{3e}} \tilde{A}_x^s = \frac{1}{6} \begin{pmatrix} -3 & 4 & -1 \\ -4 & 0 & 4 \\ 1 & -4 & 3 \end{pmatrix} \begin{pmatrix} \tilde{A}_{xi}^s \\ \tilde{A}_{xj}^s \\ \tilde{A}_{xm}^s \end{pmatrix}. \tag{C4}$$

4) The fourth element integral form in equation 17 is

$$\int_e N_i \frac{\partial \tilde{\sigma}^p}{\partial z} \tilde{A}_z^s \,\mathrm{d}z = \mathbf{K_{4e}} \tilde{A}_{ze}^s = \frac{l}{30} \begin{pmatrix} k_{11}^{4e} & k_{12}^{4e} & k_{13}^{4e} \\ k_{21}^{4e} & k_{22}^{4e} & k_{23}^{4e} \\ k_{31}^{4e} & k_{32}^{4e} & k_{33}^{4e} \end{pmatrix} \begin{pmatrix} \tilde{A}_{zj}^s \\ \tilde{A}_{zp}^s \\ \tilde{A}_{zm}^s \end{pmatrix}. \tag{C5}$$

Where,

$$\begin{aligned} &k_{11}^{4e} = -10\tilde{\sigma}_j^p + 12\tilde{\sigma}_p^p - 2\tilde{\sigma}_m^p; \quad k_{12}^{4e} = -6\tilde{\sigma}_j^p + 8\tilde{\sigma}_p^p - 2\tilde{\sigma}_m^p; \quad k_{13}^{4e} = \tilde{\sigma}_j^p - \tilde{\sigma}_m^p; \\ &k_{21}^{4e} = -6\tilde{\sigma}_j^p + 8\tilde{\sigma}_p^p - 2\tilde{\sigma}_m^p; \quad k_{22}^{4e} = -16\tilde{\sigma}_j^p + 16\tilde{\sigma}_m^p; \quad k_{23}^{4e} = 2\tilde{\sigma}_j^p - 8\tilde{\sigma}_p^p + 6\tilde{\sigma}_m^p; \\ &k_{31}^{4e} = \tilde{\sigma}_j^p - \tilde{\sigma}_m^p; \quad k_{32}^{4e} = 2\tilde{\sigma}_j^p - 8\tilde{\sigma}_p^p + 6\tilde{\sigma}_m^p; \quad k_{33}^{4e} = 2\tilde{\sigma}_j^p - 12\tilde{\sigma}_p^p + 10\tilde{\sigma}_m^p. \end{aligned}$$

5) The fifth element integral form in equation 17 is

$$\int_e \tilde{\sigma}^p \tilde{\Phi}^s N_i \,\mathrm{d}z = \mathbf{K_{5e}} \tilde{A}_{ze}^s = \frac{l}{420} \begin{pmatrix} k_{11}^{5e} & k_{12}^{5e} & k_{13}^{5e} \\ k_{21}^{5e} & k_{22}^{5e} & k_{23}^{5e} \\ k_{31}^{5e} & k_{32}^{5e} & k_{33}^{5e} \end{pmatrix} \begin{pmatrix} \tilde{\Phi}_j^s \\ \tilde{\Phi}_p^s \\ \tilde{\Phi}_m^s \end{pmatrix}. \tag{C6}$$

Where,

$$\begin{aligned} &k_{11}^{5e} = 39\tilde{\sigma}_j^p + 20\tilde{\sigma}_p^p - 3\tilde{\sigma}_m^p; \quad k_{12}^{5e} = 20\tilde{\sigma}_j^p + 16\tilde{\sigma}_p^p - 8\tilde{\sigma}_m^p; \quad k_{13}^{5e} = -3\tilde{\sigma}_j^p - 8\tilde{\sigma}_p^p - 3\tilde{\sigma}_m^p; \\ &k_{21}^{5e} = 20\tilde{\sigma}_j^p + 16\tilde{\sigma}_p^p - 8\tilde{\sigma}_m^p; \quad k_{22}^{5e} = 16\tilde{\sigma}_j^p + 192\tilde{\sigma}_p^p + 16\tilde{\sigma}_m^p; \quad k_{23}^{5e} = -8\tilde{\sigma}_j^p + 16\tilde{\sigma}_p^p + 20\tilde{\sigma}_m^p; \\ &k_{31}^{5e} = -3\tilde{\sigma}_j^p - 8\tilde{\sigma}_p^p - 3\tilde{\sigma}_m^p; \quad k_{32}^{5e} = -8\tilde{\sigma}_j^p + 16\tilde{\sigma}_p^p + 20\tilde{\sigma}_m^p; \quad k_{33}^{5e} = -3\tilde{\sigma}_j^p + 20\tilde{\sigma}_p^p + 39\tilde{\sigma}_m^p. \end{aligned}$$

6) The sixth element integral form in equation 17 is

$$\int_e N_i \frac{\partial \tilde{\sigma}^p}{\partial z} \frac{\partial \tilde{\Phi}^s}{\partial z} \,\mathrm{d}z = \mathbf{K_{6e}} \tilde{\Phi}_e^s = \frac{1}{30l} \begin{pmatrix} k_{11}^{6e} & k_{12}^{6e} & k_{13}^{6e} \\ k_{21}^{6e} & k_{22}^{6e} & k_{23}^{6e} \\ k_{31}^{6e} & k_{32}^{6e} & k_{33}^{6e} \end{pmatrix} \begin{pmatrix} \tilde{\Phi}_j^s \\ \tilde{\Phi}_p^s \\ \tilde{\Phi}_m^s \end{pmatrix}. \tag{C7}$$

Where,

$$\begin{aligned} &k_{11}^{6e} = 37\tilde{\sigma}_j^p + 36\tilde{\sigma}_p^p - 3\tilde{\sigma}_m^p; \quad k_{12}^{6e} = -6\tilde{\sigma}_j^p + 8\tilde{\sigma}_p^p - 2\tilde{\sigma}_m^p; \quad k_{13}^{6e} = -6\tilde{\sigma}_j^p + 8\tilde{\sigma}_p^p - 2\tilde{\sigma}_m^p; \\ &k_{21}^{6e} = -44\tilde{\sigma}_j^p - 32\tilde{\sigma}_p^p - 4\tilde{\sigma}_m^p; \quad k_{22}^{6e} = 48\tilde{\sigma}_j^p + 64\tilde{\sigma}_p^p + 48\tilde{\sigma}_m^p; \quad k_{23}^{6e} = 2\tilde{\sigma}_j^p - 8\tilde{\sigma}_p^p + 6\tilde{\sigma}_m^p; \\ &k_{31}^{6e} = 7\tilde{\sigma}_j^p - 4\tilde{\sigma}_p^p + 7\tilde{\sigma}_m^p; \quad k_{32}^{6e} = -4\tilde{\sigma}_j^p - 32\tilde{\sigma}_p^p - 44\tilde{\sigma}_m^p; \quad k_{33}^{6e} = -3\tilde{\sigma}_j^p + 36\tilde{\sigma}_p^p + 37\tilde{\sigma}_m^p. \end{aligned}$$

7) The seventh element integral form in equation 17 is

$$\int_e \tilde{\sigma}^p N_i \frac{\partial \tilde{\Phi}^s}{\partial z} \,\mathrm{d}z = \mathbf{K_{7e}} \tilde{\Phi}_e^s = \frac{1}{30} \begin{pmatrix} k_{11}^{7e} & k_{12}^{7e} & k_{13}^{7e} \\ k_{21}^{7e} & k_{22}^{7e} & k_{23}^{7e} \\ k_{31}^{7e} & k_{32}^{7e} & k_{33}^{7e} \end{pmatrix} \begin{pmatrix} \tilde{\Phi}_j^s \\ \tilde{\Phi}_p^s \\ \tilde{\Phi}_m^s \end{pmatrix}. \tag{C8}$$

Where,

$$k_{11}^{7e} = -10\tilde{\sigma}_j^p - 6\tilde{\sigma}_p^p + \tilde{\sigma}_m^p; \quad k_{12}^{7e} = 12\tilde{\sigma}_j^p + 8\tilde{\sigma}_p^p; \quad k_{13}^{7e} = -2\tilde{\sigma}_j^p - 2\tilde{\sigma}_p^p - \tilde{\sigma}_m^p;$$

607 $$k_{21}^{7e} = -6\tilde{\sigma}_j^p - 16\tilde{\sigma}_p^p + 2\tilde{\sigma}_m^p; \quad k_{22}^{7e} = 8\tilde{\sigma}_j^p - 8\tilde{\sigma}_m^p; \quad k_{23}^{7e} = -2\tilde{\sigma}_j^p + 16\tilde{\sigma}_p^p + 6\tilde{\sigma}_m^p;$$

$$k_{31}^{7e} = 7\tilde{\sigma}_j^p - 4\tilde{\sigma}_p^p + 7\tilde{\sigma}_m^p; \quad k_{32}^{7e} = -8\tilde{\sigma}_p^p - 12\tilde{\sigma}_m^p; \quad k_{33}^{7e} = -\tilde{\sigma}_j^p + 6\tilde{\sigma}_p^p + 10\tilde{\sigma}_m^p.$$

608

609 REFERENCES

610 Ansari, S., and C. Farquharson, 2014, 3D finite-element forward modeling of
611 electromagnetic data using vector and scalar potentials and unstructured grids:
612 GEOPHYSICS, **79**, E149–E165.

613 Avdeev, D., and A. Avdeeva, 2009, 3D magnetotelluric inversion using a limited-
614 memory quasi-Newton optimization: GEOPHYSICS, **74**, F45–F57.

615 Avdeev, D. B., A. V. Kuvshinov, O. V. Pankratov, and G. A. Newman, 1997, High-
616 Performance Three-Dimensional Electromagnetic Modelling Using Modified
617 Neumann Series. Wide-Band Numerical Solution and Examples: Journal of
618 Geomagnetism and Geoelectricity, **49**, 1519–1539.

619 Avdeev, D. B., A. V. Kuvshinov, O. V. Pankratov, and G. A. Newman, 2002, Three-
620 dimensional induction logging problems, Part I: An integral equation solution and
621 model comparisons: GEOPHYSICS, **67**, 413–426.

622 Ayachit, U., 2020, The ParaView Guide: , 276.

623 Badea, E. A., M. E. Everett, G. A. Newman, and O. Biro, 2001, Finite-element analysis
624 of controlled-source electromagnetic induction using Coulomb-gauged potentials:
625 GEOPHYSICS, **66**, 786–799.

626 Chai, Y., 2009, A-E equation of potential field transformations in the wavenumber
627 domain and its application: Applied Geophysics, **6**, 205–216.

628 Chen, H., and T. Li, 2019, 3-D marine controlled-source electromagnetic modelling in
629 an anisotropic medium using a Wavelet–Galerkin method with a secondary potential
630 formulation: Geophysical Journal International, **219**, 373–393.

631 Dai, S., D. Zhao, S. Wang, B. Xiong, Q. Zhang, K. Li, L. Chen, and Q. Chen, 2019,
632 Three-dimensional numerical modeling of gravity and magnetic anomaly in a mixed
633 space-wavenumber domain: GEOPHYSICS, **84**, G41–G54.
634 Egbert, G., and A. Kelbert, 2012, Computational recipes for electromagnetic inverse
635 problems: Geophysical Journal International, **189**, 251–267.
636 Farquharson, C. G., and M. P. Miensopust, 2011, Three-dimensional finite-element
637 modelling of magnetotelluric data with a divergence correction: Journal of Applied
638 Geophysics, **75**, 699–710.
639 Franke, A., R.-U. Börner, and K. Spitzer, 2007, 3D finite element simulation of
640 magnetotelluric fields using unstructured grids: , 4.
641 Gao, G., 2005, Simulation of borehole electromagnetic measurements in dipping and
642 anisotropic rock formations and inversion of array induction data.Thesisp.
643 Grayver, A. V., and T. V. Kolev, 2015, Large-scale 3D geoelectromagnetic modeling
644 using parallel adaptive high-order finite element methodEM modeling with high-order
645 FEM: Geophysics, **80**, E277–E291.
646 Haber, E., and U. M. Ascher, 2001, Fast Finite Volume Simulation of 3D
647 Electromagnetic Problems with Highly Discontinuous Coefficients: SIAM Journal on
648 Scientific Computing, **22**, 1943–1961.
649 Haber, E., U. M. Ascher, D. A. Aruliah, and D. W. Oldenburg, 2000, Fast Simulation of
650 3D Electromagnetic Problems Using Potentials: Journal of Computational Physics, **163**,
651 150–171.
652 Hursán, G., and M. S. Zhdanov, 2002, Contraction integral equation method in three-

653 dimensional electromagnetic modeling: Radio Science, **37**, 1–13.
654 Jahandari, H., and C. G. Farquharson, 2014, A finite-volume solution to the geophysical
655 electromagnetic forward problem using unstructured grids: GEOPHYSICS, **79**, E287–
656 E302.
657 Jahandari, H., and C. G. Farquharson, 2015, Finite-volume modelling of geophysical
658 electromagnetic data on unstructured grids using potentials: Geophysical Journal
659 International, **202**, 1859–1876.
660 Jahandari, H., and C. G. Farquharson, 2017, 3-D minimum-structure inversion of
661 magnetotelluric data using the finite-element method and tetrahedral grids:
662 Geophysical Journal International, **211**, 1189–1205.
663 Jahandari, H., S. Ansari, and C. G. Farquharson, 2017, Comparison between staggered
664 grid finite–volume and edge–based finite–element modelling of geophysical
665 electromagnetic data on unstructured grids: Journal of Applied Geophysics, **138**, 185–
666 197.
667 Jin, J.-M., 2015, The Finite Element Method in Electromagnetics: John Wiley & Sons.
668 Key, K., 2016, MARE2DEM: a 2-D inversion code for controlled-source
669 electromagnetic and magnetotelluric data: Geophysical Journal International, **207**, 571–
670 588.
671 Liu, C., Z. Ren, J. Tang, and Y. Yan, 2008, Three-dimensional magnetotellurics
672 modeling using edge-based finite-element unstructured meshes: Applied Geophysics,
673 **5**, 170–180.
674 Lynch, D. R., and K. D. Paulsen, 1991, Origin of vector parasites in numerical Maxwell

675 solutions: IEEE Transactions on Microwave Theory and Techniques, **39**, 383–394.
676 Mackie, R. L., J. T. Smith, and T. R. Madden, 1994, Three-dimensional electromagnetic
677 modeling using finite difference equations: The magnetotelluric example: Radio
678 Science, **29**, 923–935.
679 Mitsuhata, Y., and T. Uchida, 2004, 3D magnetotelluric modeling using the T-Ω finite-
680 element method: GEOPHYSICS, **69**, 108–119.
681 Mukherjee, S., and M. E. Everett, 2011, 3D controlled-source electromagnetic edge-
682 based finite element modeling of conductive and permeable heterogeneities:
683 GEOPHYSICS, **76**, F215–F226.
684 Nam, M. J., H. J. Kim, Y. Song, T. J. Lee, J.-S. Son, and J. H. Suh, 2007, 3D
685 magnetotelluric modelling including surface topography: Geophysical Prospecting, **55**,
686 277–287.
687 Newman, G., and D. Alumbaugh, 2000, Three-dimensional magnetotelluric inversion
688 using non-linear conjugate gradients: Geophysical Journal International, **140**, 410–424.
689 Newman, G. A., and D. L. Alumbaugh, 1995, Frequency-domain modelling of airborne
690 electromagnetic responses using staggered finite differences1: Geophysical
691 Prospecting, **43**, 1021–1042.
692 Ren, Z., T. Kalscheuer, S. Greenhalgh, and H. Maurer, 2013, A goal-oriented adaptive
693 finite-element approach for plane wave 3-D electromagnetic modelling: Geophysical
694 Journal International, **194**, 700–718.
695 Saad, Y., 2003, Iterative Methods for Sparse Linear Systems: Society for Industrial and
696 Applied Mathematics.

Sasaki, Y., 2001, Full 3-D inversion of electromagnetic data on PC: Journal of Applied Geophysics, **46**, 45–54.

Shen, J., 2003, Modeling of 3-D Electromagnetic Responses in Frequency domain by Using the Staggeredgrid Finite Difference Method: Chinese Journal of Geophysics, **46**, 396–408.

Si, H., 2015, TetGen, a Delaunay-Based Quality Tetrahedral Mesh Generator: ACM Transactions on Mathematical Software, **41**, 11:1-11:36.

da Silva, N. V., J. V. Morgan, L. MacGregor, and M. Warner, 2012, A finite element multifrontal method for 3D CSEM modeling in the frequency domain: GEOPHYSICS, **77**, E101–E115.

Smith, J. T., 1996, Conservative modeling of 3-D electromagnetic fields, Part II: Biconjugate gradient solution and an accelerator: GEOPHYSICS, **61**, 1319–1324.

Streich, R., 2009, 3D finite-difference frequency-domain modeling of controlled-source electromagnetic data: Direct solution and optimization for high accuracy: GEOPHYSICS, **74**, F95–F105.

Sugeng, F., 1998, Modeling the 3D TDEM response using the 3D full-domain finite-element method based on the hexahedral edge-element technique: Exploration Geophysics, **29**, 615–619.

Tontini, F. C., L. Cocchi, and C. Carmisciano, 2009, Rapid 3-D forward model of potential fields with application to the Palinuro Seamount magnetic anomaly (southern Tyrrhenian Sea, Italy): Journal of Geophysical Research: Solid Earth, **114**.

Um, E. S., D. L. Alumbaugh, and J. M. Harris, 2010, A Lorenz?gauged finite?element

719 solution for transient CSEM modeling, *in* SEG Technical Program Expanded Abstracts
720 2010, , . SEG Technical Program Expanded AbstractsSociety of Exploration
721 Geophysicists, 748–752.
722 Varentsov, Iv. M., 1983, Modern trends in the solution of forward and inverse 3D
723 electromagnetic induction problems: Geophysical Surveys, **6**, 55–78.
724 Varilsuha, D., and M. E. Candansayar, 2018, 3D magnetotelluric modeling by using
725 finite-difference method: Comparison study of different forward modeling approaches:
726 GEOPHYSICS, **83**, WB51–WB60.
727 Wannamaker, P., G. Hohmann, and S. Ward, 1984a, Magnetotelluric responses of three-
728 dimensional bodies in layered earths: GEOPHYSICS, **49**, 1517–1533.
729 Wannamaker, P. E., G. W. Hohmann, and W. A. SanFilipo, 1984b, Electromagnetic
730 modeling of three-dimensional bodies in layered earths using integral equations:
731 GEOPHYSICS, **49**, 60–74.
732 Wu, L., and G. Tian, 2014, High-precision Fourier forward modeling of potential fields:
733 GEOPHYSICS, **79**, G59–G68.
734 Xu, S., 1994, The Finite Element Method in Geophysics: Science Press.
735 Zhdanov, M. S., 2010, Electromagnetic geophysics: Notes from the past and the road
736 ahead: GEOPHYSICS, **75**, 75A49-75A66.
737 Zhdanov, M. S., S. K. Lee, and K. Yoshioka, 2006, Integral equation method for 3D
738 modeling of electromagnetic fields in complex structures with inhomogeneous
739 background conductivity: GEOPHYSICS, **71**, G333–G345.
740 Zunoubi, M. R., Jian-Ming Jin, K. C. Donepudi, and Weng Cho Chew, 1999, A spectral

741 Lanczos decomposition method for solving 3-D low-frequency electromagnetic
742 diffusion by the finite-element method: IEEE Transactions on Antennas and
743 Propagation, **47**, 242–248.
744

745 Figure and Table Captions

746

747 **Figure 1.** Synthetic resistivity model. A 10 Ωm anomaly is buried at 0.2 km depth in a
748 100 Ωm half-space model. The model region is 2×2×0.7 km^3 and the volume of the
749 conductive anomaly is 0.8×0.4×0.4 km^3. The resistivities of the background half-space,
750 the anomaly, and the air are 100, 10, and 10^8 Ωm, respectively.

751

752 **Figure 2.** The fitting error against iteration number for the iterative approximation of
753 the electric field. The YX mode (*y* direction polarization) seems more stable than the
754 XY mode (*x* direction polarization).

755

756 **Figure 3.** Apparent resistivities and phases at the frequency of 10 Hz calculated via
757 the proposed algorithm, the IE algorithm, and the relative differences of the two along
758 the plane of z = 0, (a) ρ_{xy}, (b) ρ_{yx}, (c) φ_{xy}, and (d) φ_{yx}. The relative differences are
759 smaller than typical noise levels in field data.

760

761 **Figure 4.** The relative differences of apparent resistivities and phases along the
762 central profile marked in Figure 1, (a) ρ_{xy}, (b) ρ_{yx}, (c) φ_{xy}, and (d) φ_{yx}.

763

764 **Figure 5.** The 3D model modified after Zhdanov et al. (2006). The volume of each
765 anomaly is 0.4×0.4×0.4 km^3, and the top of the anomaly body is located at 0.2 km
766 depth. The resistivities of the background, the conductive anomaly, the resistive

anomaly, and the air are 100, 10, 1000, and 10^8 Ωm, respectively.

Figure 6. Apparent resistivities and phases at the frequency of 0.1 Hz calculated via the proposed algorithm and the algorithm of Ren et al. (2013) along the *x* axis, (a) ρ_{xy}, (b) φ_{xy}, (c) ρ_{yx}, and (d) φ_{yx}. The corresponding relative differences of the two solutions are shown in (e) - (h). The differences generally are within 5% except at a few data points.

Figure 7. A sphere model used for the modelling efficiency study. Paraview is used for visualization (Ayachit, 2020). Only one-quarter of the model is shown for ease of visual inspection. The anomaly is an approximate sphere with a radius of about 0.4 km. Its resistivity is 1000 Ωm. The resistivities of background and air are 100 and 10^8 Ωm, respectively.

Figure 8. Apparent resistivities and phases at the frequency of 1 Hz calculated via the proposed algorithm, the FEM algorithm of Jahandari and Farquharson (2017), and the relative differences of the two along the plane of z = 0, (a) ρ_{xy}, (b) ρ_{yx}, (c) φ_{xy}, and (d) φ_{yx}. The relative differences are smaller than typical noise levels in field data.

Table 1. The symbols used for different parameters in the spatial domain and the mixed space-wavenumber domain are listed.

789

790